Impurity temperatures measured via line shape analysis in the island scrape-off-layer of Wendelstein 7-X

To cite this article: D Gradic *et al* 2022 *Plasma Phys. Control. Fusion* **64** 075010

OPEN ACCESS
IOP Publishing
Plasma Physics and Controlled Fusion
Plasma Phys. Control. Fusion **64** (2022) 075010 (14pp)
https://doi.org/10.1088/1361-6587/ac70fa

Impurity temperatures measured via line shape analysis in the island scrape-off-layer of Wendelstein 7-X

D Gradic*, M Krychowiak, R König, F Henke, M Otte, V Perseo, T Sunn Pedersen and W7-X Team[1]

Max-Planck-Institut für Plasmaphysik, Teilinstitut Greifswald, D-17491 Greifswald, Germany

E-mail: dorothea.gradic@ipp.mpg.de

Received 12 January 2022, revised 28 April 2022
Accepted for publication 18 May 2022
Published 7 June 2022

Abstract

Impurity temperatures have been determined by a spectroscopic line shape analysis for several species in the divertor scrape-off-layer of the stellarator Wendelstein 7-X (W7-X). Examples include spectral lines from intrinsic elements (C II and C III, He I) as well as from seeded impurities (Ar II, N II) through the divertor gas inlet system. Both Doppler broadening and Zeeman splitting are found to contribute significantly to the impurity line shapes. Zeeman splitting arises due to the confining magnetic field in W7-X and complicates the line shape appearance. By attributing Doppler widths to each of the various Zeeman components, however, we demonstrate that reliable ion temperature values can be derived provided that the presence of the magnetic field is properly accounted for. The spectrally highly resolved lines are analyzed by means of a multi-parameter, least-squares fit routine, which accounts for Doppler broadening, Zeeman splitting, as well as the instrumental broadening of the spectrometer used to measure the spectral line shapes. By spectral fitting of the Zeeman features, it is also found that the line shape analysis can yield values for the local magnetic field, which can be used to localize the impurity radiation approximately provided that the line emission is dominant in a small area intersected by the lines of sight of the spectrometer.

Keywords: impurity temperatures, Doppler broadening, Zeeman splitting

(Some figures may appear in colour only in the online journal)

1. Introduction

Assessing the impurity behavior in the scrape-off-layer (SOL) is one of the fundamental tasks for edge spectroscopy in high-temperature plasma experiments. Impurity distribution, flow dynamics and temperatures as well as the degree of sputtering and erosion at the divertor targets characterize the amount of impurities transported into the confined plasma core. Impurity radiation also plays an important role in inducing detachment of the SOL plasma at the targets. The study, understanding and prediction of the impurity edge behavior is therefore crucial for the successful operation of high-temperature plasma experiments and future fusion power plants. Moreover, source distributions and acting forces (cf [1]) can lead to significant differences between the flow dynamics and temperatures of the main exhaust plasma ions and impurities in the SOL. This necessitates a careful distinction between their parameters for e.g. accurate simulations of the plasma wall interactions.

In the plasma boundary of tokamaks, the ion temperature, T_i, of the main exhaust plasma species is usually measured to

[1] See Klinger *et al* 2019 (https://doi.org/10.1088/1741-4326/ab03a7) for the W7-X Team.

* Author to whom any correspondence should be addressed.

be higher than the electron temperature [2, 3]. In conduction and sheath-limited SOLs, the ion parallel heat conductivity is much smaller than that of the electrons, which leads to $T_i > T_e$ if electron and ions are thermally decoupled along the open magnetic field lines. Thermal equilibrium can only be achieved if the ion transit time parallel to the field lines ($\tau_{p,\parallel} \propto L_c/\sqrt{T_i + T_e}$) is greater than the ion-electron thermalization time ($\tau_{i,e} \propto T_e^{3/2}/n_e$) [2]. In a similar fashion, impurity temperatures are also dependent on the lifetime and thermalization rates of excited transitions in the SOL. The temperatures of the lower ionization stages depend upon the ratio of two collision rates: that of elastic (momentum changing) collisions with the background protons (deuterons) to the rate of ionization by electron impact. Therefore, they can vary substantially from the background proton or deuterium temperature [4, 5].

Spectroscopic diagnostics have the key advantage to be able to identify and differentiate between the various impurity species and charge stages by the detection of atomic emission line spectra. They allow one to derive many important plasma parameters with several commonly established methods such as line ratio analysis (T_e, n_e) [6, 7], absolute total line intensity measurements (impurity concentrations) [7] or the detection of broadband continuum bremsstrahlung (Z_{eff}) [8]. These methods can usually be performed with low- to medium-wavelength resolution spectrometers. Further methods such as (active) charge exchange emission spectroscopy [9] or spectral line broadening analysis [10] are commonly used in the hot core plasma for measuring impurity densities, ion temperatures, T_i, and ion velocities, v_i. In the relatively cold plasma edge ($T_i < 100\,\mathrm{eV}$), these methods can be applied as well; however, they require significantly higher wavelength resolution spectrometers due to the narrow widths of the emitted spectral lines.

This paper presents a first line-broadening analysis of several atomic impurity lines emitted in the island divertor of the optimized stellarator Wendelstein 7-X (W7-X). The present goal is to assess the temperature and distribution of ion impurity species in low ionization states and to demonstrate the validity of the applied line shape analysis itself. Depending on the atomic emission species and location in the plasma, several physics effects can contribute to the spectral line shape:

- Doppler broadening (dependent on T_i of the ion species),
- fine-structure splitting,
- Zeeman splitting pattern ($\vec{B}$) and
- Stark broadening (n_e).

Thermal Doppler broadening is characterized by Gaussian line shapes and depends on the emitting impurity species temperature. The individual fine-structure splitting of each spectral transition is altered by the Zeeman effect, which is caused by the confining magnetic field of W7-X ($B \approx 2.5$ T on axis). In the SOL, the effective line broadening by Zeeman splitting is of the same order as the Doppler broadening for many spectral lines [11]. This is why Zeeman-broadened spectra are rich in additional features, which may help for identification of the transitions, and have to be considered for accurately analyzing the spectral line shapes. In general, for magnetic fields of the order of 2.5 T, high-wavelength resolution spectrometers are required for resolving the Zeeman features. The spectrometer used for the line broadening analysis in this paper is introduced in section 2. The line broadening analysis is made by a multi-parameter fitting routine, which is described in section 3. Examples of measured spectra and their derived impurity temperatures are presented in section 4. The line broadening analysis also yields values for the magnetic field strength, B, and the observation angle, θ, between the sightline and magnetic field vector linked to the Zeeman effect. In section 5, we shall discuss the possibility to use these magnetic field parameters for localizing the emission species along the spectrometer lines of sight (LOS), followed by a summary and conclusions in chapter 6.

Stark broadening depends on the plasma density and is characterized by a Lorentzian line shape. In W7-X, this broadening process is only observed for hydrogen Balmer lines, which are not investigated in this article.

2. The high-resolution spectrometer on W7-X

In order to perform passive line broadening analysis for visible emission lines in the SOL of W7-X, a large Ebert–Fastie Echelle spectrograph (focal length $F = 1150\,\mathrm{mm}$) was used due to its high spectral resolution. Figure 1 shows a schematic of the monochromator (Sopra UHRS-F.1150). It is characterized by one large concave mirror and a moveable Echelle grating with a groove density of $N = 324\,\mathrm{grooves\,mm^{-1}}$ for selecting a spectral wavelength range. The grating drive is controlled by a sine arm made of invar for thermal stability. The Ebert angle is $\epsilon = 6.5°$ and the fundamental wavelength of the system was set to $\lambda_f = 5570$ nm. For more specific information on the Ebert–Fastie configuration, the reader may consult [12].

A prism is used to pre-select a single spectral order in the pre-monochromator. Since the Echelle spectrograph is operated in high spectral order (usually 10–14), the pre-monochromator avoids an overlapping of several spectral orders in the detector camera. At the pre-monochromator entrance, 60 optical fibers with a diameter of 165 μm (silica core and cladding) are arranged in a vertical row, to mimic an entrance slit for the pre-monochromator. In addition, one overview fiber with 1 mm diameter is arranged below the 60 thin fibers. The spectrometer is located on an optical table in a spectroscopy laboratory, which receives light from the W7-X torus by long optical fiber bundles (70–100 m in length). Via a patch panel, the spectrometer fibers are connected to observation fibers in various view ports in W7-X, allowing the user to switch the LOS into the device during the plasma campaign.

The Ebert–Fastie spectrograph is characterized by good wavelength tuning capability and ultra-high spectral resolution. In comparison to the Czerny-Turner set-up, only one large concave mirror is applied instead of two, resulting in a symmetric arrangement of the components with less degrees of freedom. This is why the Ebert–Fastie set-up yields high stability, which is important for systems with high F number. The exposure times are on the order of typically several hundreds

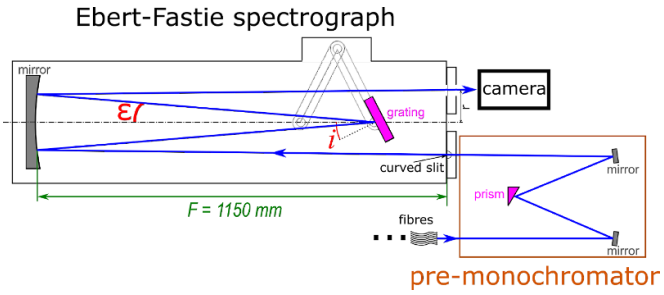

Figure 1. A schematic of the high resolution Echelle spectometer used for the line broadening analysis in W7-X. The light from W7-X (in blue) is transported via optical fibers and enters the spectrograph through a pre-monochromator (orange). In the spectrograph, the light is reflected and diffracted onto the camera detector by a fixed concave mirror and a fine-tuneable grating, which is driven on a sine arm (in grey).

of milliseconds in the applied set-up for W7-X, depending on the observed emission line intensity and the selected width of the entrance slit between the spectrograph and the pre-monochromator. Characteristic parameters, such as the dispersion and instrument function, as well as the view into W7-X will be described in more detail in the next subsections.

2.1. Spectrometer dispersion

Due to the Ebert–Fastie spectrograph's large focal length, F, a very high spectral dispersion is achieved, according to:

$$\texttt{dispersion coefficient} = \frac{\lambda}{F \cdot \tan(i)} \cdot \frac{13}{2} \qquad (1)$$

where

$$i = \sin^{-1}\left(\frac{k \cdot N \cdot \lambda}{2 \cdot \cos(\epsilon)}\right) \qquad (2)$$

is the angle between the grating normal and the central axis of the mirror (cf figure 1). Figure 2 illustrates the wavelength dispersion of the high-resolution spectrometer in the visible spectral range. Each jump in the dispersion curve marks a change of the spectral order $k = \lambda_f/\lambda$ (rounded). For the chosen setting of spectrometer parameters (ε, λ_f), the spectral order varies between $k = 14$ to $k = 8$ in the visible range. The dispersion varies between 0.7 to 2.5 pm/camera pixel, resulting in a spectral range of 1–3 nm over the detector camera (with 1024 $\times$ 1024 pixels, 13 μm $\times$ 13 μm pixel size), depending on the wavelength setting of the spectrometer. Usually, this range is only sufficient to detect one or two very close atomic emission lines at a single wavelength setting, albeit with very high spectral resolution.

The values of ε, λ_f and the dispersion of the spectrometer were determined by wavelength scans (see black markers in figure 2) with a fine-tuneable OPO laser, C-WAVE, in combination with a high-precision wavemeter. During the OPO laser scans, the wavelength was varied in steps of 5 pm in a range of 60 picometres (the fine-tuned OPO laser scans are described in [13, 14] in more detail). The scans were performed at four

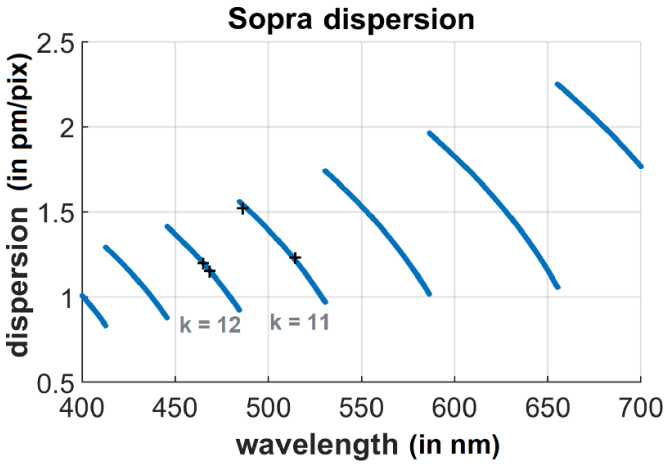

Figure 2. Simulated dispersion curve of the high-wavelength resolution spectrometer (in blue) and measured dispersion values (black markers). Two values of the spectral order k are given for orientation.

different spectrometer settings to collect a set of data points, to which the spectrometer dispersion curve could be fitted with good agreement.

2.2. Wavelength calibration and curved-slit effect

Due to the high spectral resolution of the Echelle spectrometer, not only line broadening analysis, but also the detection of Doppler shifts of the order of a few picometres becomes possible. However, for absolute velocity measurements based on the Doppler line shifts, a wavelength calibration of the spectrometer is required. Since the visible detection range of the Echelle spectrometer is relatively small (1–3 nm), spectral lamps alone cannot always be used where a Doppler shift analysis is desired. For example, for measuring the C III multiplet around 465 nm, where the spectral resolution is 1.2 pm/pix and the detection range of the camera corresponds to 1.2 nm, an intense spectral lamp line is not available for direct calibration. The closest, sufficiently intense lamp line is the Zn I line at 468.0135 nm, well outside the wavelength range of the spectrometer. Instead, wavelength calibration is carried out with the fine-tuneable OPO laser C-WAVE [14], which can be steered to the unshifted center of mass of the C III multiplet around 464.8811 nm (wavelength in air), inside the spectrometer range.

When measuring monochromatic lines of spectral lamps or lasers, two effects are observed for the spectrometer:

(a) By changing the wavelength setting back and forth, the same wavelength position on the camera chip can vary by $\pm$15 pixels.
(b) For the projected fiber channels on the camera chip, the same wavelength does not appear at the same x-pixel, but varies slightly.

Concerning the first point, the variation of the wavelength setting by a few camera pixels (which corresponds to a few picometres) means that wavelength calibrations are necessary

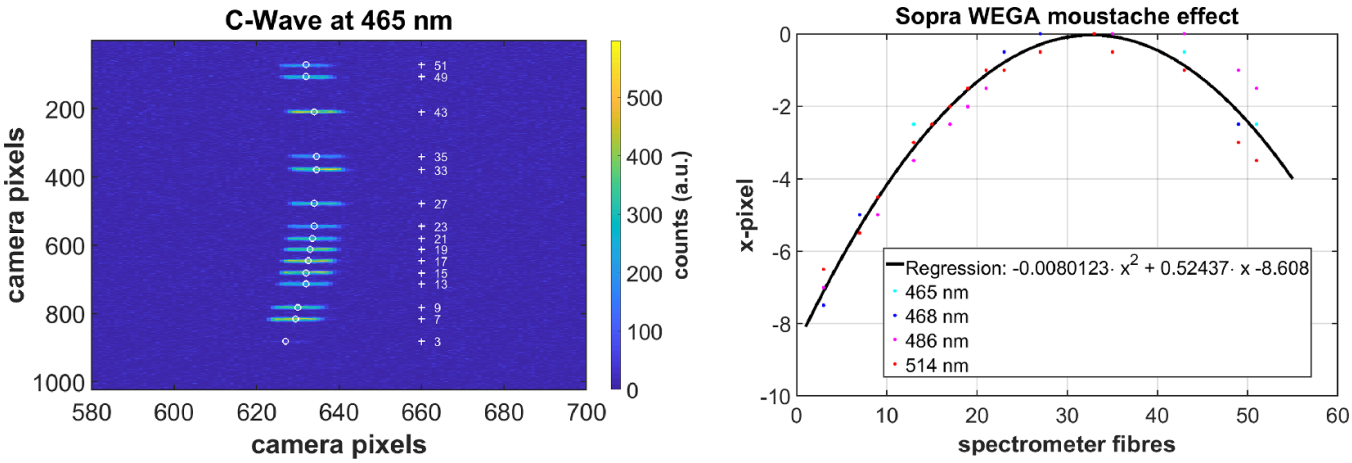

Figure 3. Left: measured instrument widths in various channels on the (unbinned) spectrometer camera chip, partially zoomed in over the x-axis. The channels were illuminated by a monochromatic light source (C-WAVE laser at 464.8811 nm) and display the same wavelength at slightly different positions over the x-axis of the camera chip. Right: measured x-positions of four different monochromatic wavelengths in the retrospectively binned spectrometer sightline channels (colored markers). The black curve shows the 2nd order polynomial regression fit of the curved slit effect measured over all four different wavelengths.

after each change of the spectrometer settings. Wavelength calibrations can even become necessary at the same setting if air conditions in the spectrometer laboratory change, because of the wavelength dependence on air pressure and temperature. This is why wavelength calibrations were usually performed directly before or after each W7-X plasma discharge for the Echelle spectrometer.

Concerning the second point, the Ebert–Fastie spectrograph is characterized by a 'curved slit' image or 'moustache' effect, illustrated in the left image of figure 3. The vertical row of the entrance fibers are at different positions (sightline channels) on the y-axis of the spectrometer camera chip. The x-direction represents the wavelength. The same wavelength appears at different x-pixels for each fiber channel, which results in a variation of the projected wavelength positions over the camera chip, resembling a slight curve with a large radius. Over all 60 channels of the camera, the variation can be up to 8 pixels (or 9.6 pm at a spectrometer setting of 465 nm). Therefore, the curved slit effect has to be considered when analyzing the Doppler shift in each channel. Since usually only one or two of the spectrometer channels are routinely connected to a wavelength calibration source, a polynomial regression fit curve was fitted to the measured positions of different monochromatic line measurements, illustrated in figure 3. Within the measurement uncertainties, the curved slit effect is the same at different wavelength settings, due to the symmetric assembly of the spherical mirror and the grating in the Ebert–Fastie configuration [12]. This is why the polynomial regression fit can be used at all wavelength settings.

2.3. *Instrument function*

The instrumental width of a spectrometer determines its spectral resolution capabilities and thus the ability to perform a line-broadening analysis for the narrow spectral lines emitted by SOL plasmas. For the Echelle spectrograph, it is primarily determined by the F-number and the width of the entrance

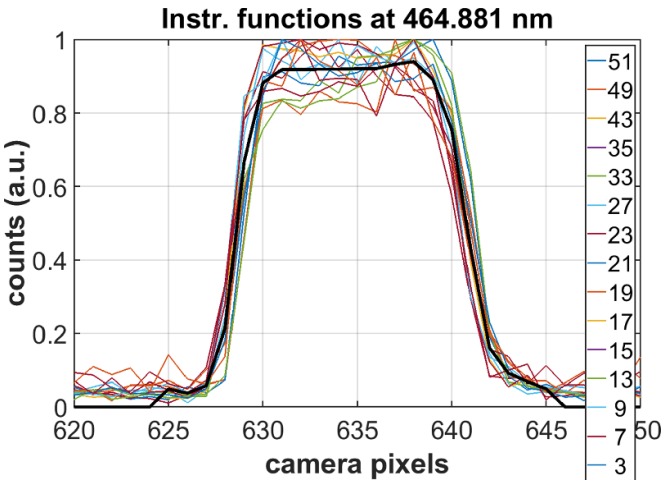

Figure 4. Measured instrument functions in different camera sightline channels (colored) and the averaged instrument function (in black).

slit, which was set to 200 μm for all spectral measurements performed during the operation phase OP1.2b of W7-X (and thus all measurements presented in this work). The instrumental width was determined with the C-WAVE laser measurements at different wavelength settings, already mentioned in sections 2.1 and 2.2. Figure 4 shows the measured instrument functions at the wavelength setting of 464.8 nm in different sightline channels of the spectrometer. The curved slit effect was corrected for the comparison, to demonstrate that the instrumental width is about the same for each sightline channel. The averaged instrumental width is approximately 15 pixels, which corresponds to 18 pm or 0.18 Å at the wavelength setting of 465 nm according to the dispersion relation (1). For comparison, thermal broadening for e.g. C II and C III lines is between $\sigma_D = \lambda \cdot \sqrt{\frac{k_B T_i}{M_{\mathrm{Nuc}} c^2}} \approx 22$ to 39 pm for an assumed temperature range of $T_{i,n} = 5$ to 15 eV ($\lambda = 450$ nm).

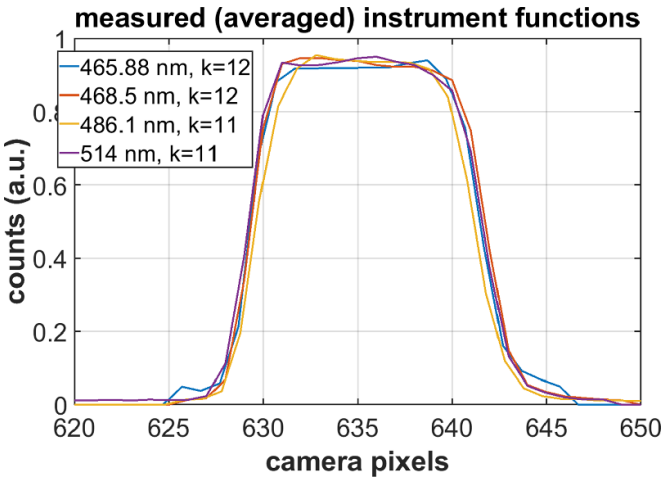

Figure 5. Averaged instrument functions measured at different wavelength settings of the high-wavelength resolution Echelle spectrometer.

Thus, the resolution of the $F = 1150$ mm Fastie spectrometer is sufficient for the line broadening analysis presented in this paper.

It was also experimentally confirmed that the instrumental width does not change significantly for other wavelength settings of the spectrometer, as shown in figure 5.

2.4. Spectrometer LOS

The LOS used by the spectrometer in the last plasma campaign, OP1.2b, view nearly vertically into one of the lower island divertors of W7-X. A schematic representation of the LOS end points on the graphite targets can be found in figures 6 and 7. The photo in figure 6 was taken after the end of the last plasma campaign, OP1.2b. The LOS positions were measured by back-illumination. The LOS are focused by a collimator lens ($f = 35$ mm) behind a vacuum window and observe the divertor over a large poloidal cross-section of the horizontal target, the pumping gap and vertical target. The length of the LOS varies between $l = 1.5$–1.7 m. As will be discussed later in more detail (cf figure 16), the LOS cross the core plasma once and the SOL twice: in front of the window as well as well as in front of the divertor. The orientation of the LOS with respect to the magnetic field topology varies between $\theta \approx 108°$–$115°$ at the targets (in the standard magnetic configuration), where most of the passive visible emission occurs in attached conditions.

3. Spectral line broadening analysis in the W7-X SOL

Due to the high spectral resolution of the Echelle spectrometer, line broadening analysis can be performed for many atomic emission lines passively radiating in the SOL of W7-X. The highly resolved spectra demonstrate that, next to thermal Doppler broadening, the Zeeman effect contributes significantly to the effective line broadening of impurity emission lines in the

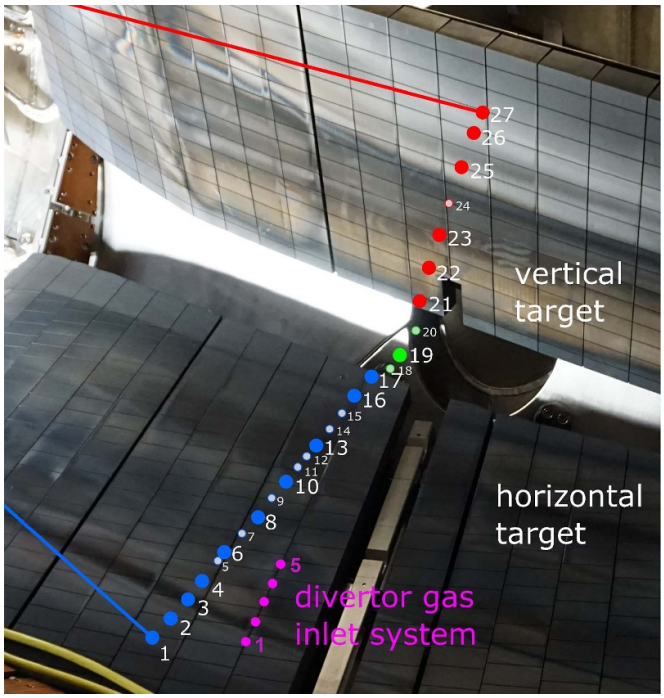

Figure 6. Overview of the spectrometer LOS into one of the lower island divertors in W7-X. Blue LOS end on the horizontal divertor target, green in the pumping gap and the red LOS end on the vertical target. The positions of the five divertor-gas-inlet nozzles are indicated in magenta.

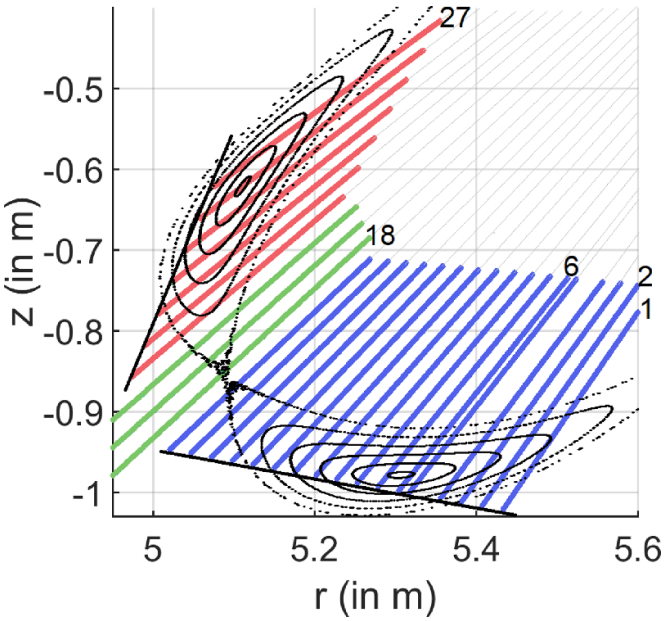

Figure 7. Fan geometry of the LOS into one of the lower island divertors in W7-X. Blue LOS end on the horizontal divertor target, green in the pumping gap and the red LOS end on the vertical target. A Poincaré plot of the SOL islands in magnetic standard configuration (EJM262 with $I_{cc} = 2$ kA) is provided as well.

visible. This is due to the relatively low SOL particle temperatures ($T_i < 100$ eV) and high confining magnetic field strength of $B \approx 2$–3 T within the SOL (cf left image in figure 16), as also

reported for the SOL of tokamaks [15]. For some atomic lines, such as the hydrogen Balmer lines, Stark broadening is significant as well. However, for most impurity lines, only Doppler broadening and the Zeeman effect play a role, which will be the main focus of the analysis performed in this work.

3.1. Fitting procedure

The highly resolved, measured impurity spectra are analyzed by means of a multi-parameter least-squares fit routine by considering

- Gaussian Doppler broadening (dependent on T_i),
- Doppler line shift (dependent on v_i),
- Zeeman splitting (dependent on the magnetic field strength, B, and the observation angle, θ, between the magnetic field vector $\vec{B}$ and the diagnostic sightline),
- instrumental broadening and
- continuum background.

The basis for determining the magnetic Zeeman effect is a code provided by John D. Hey, who applied and documented his calculations in [4, 15–17]. The routine is also implemented and accessible in the (closed) ADAS603 database [18]. It generates the Zeeman/Paschen-Back multiplet components for hydrogenic as well as non-hydrogenic spectral lines as a function of magnetic field magnitude, B, and observation angle θ. B, θ and the spectral line transition information are the input parameters. The output are the wavelength, λ_Z, and the relative intensity, I_Z, of each Zeeman split component, which are usually indicated as vertical lines in the spectral fit plots in section 4. If desired, the π and σ polarization state can be provided as well.

The main approach of the spectral simulation routine is to generate a Doppler Gaussian function,

$$G(\lambda-\lambda_Z,\sigma_D)=\frac{1}{\sqrt{2\pi}\cdot\sigma_D}\exp\left[-\frac{1}{2}\left(\frac{\lambda-\lambda_Z}{\sigma_D}\right)^2\right], \quad (3)$$

for each of the Zeeman split line components of the observed spectral line, where $W_T=\sqrt{8\ln(2)}\sigma_D$ is the full-width at half maximum of the profile, and $\sigma_D=\lambda_Z\cdot\sqrt{\frac{k_B T_i}{M_{\mathrm{Nuc1}}c^2}}$. The parameter $\lambda_Z=\lambda_0-\Delta\lambda$ is the shifted, center-of-mass wavelength of the observed multiplet component. λ_0 is the central (intensity weighted) wavelength and $\Delta\lambda=\lambda_0\cdot\frac{v_i}{c}$ is the Doppler shift, which depends on the emitting particle velocity, v_i. The velocity is assumed to be the same for each Zeeman split component. The accumulation of all Gaussian functions is numerically convoluted with the measured averaged instrument function of the spectrometer, which is described in section 2.3. To account for the continuum spectral background, which can be dependent on several physics effects such as bremsstrahlung or thermal radiation from the targets, a horizontal line is added to the simulated spectral function, which is not physically interpreted any further. A trivial horizontal line is deemed sufficient for the background due to the small detection range of the spectrometer, which is always less than 3 nm.

T_i, B and v_i are free parameters of the fit routine. Also the horizontal baseline, which is used to account for continuum background emission over the spectral detection range of the spectrometer camera, is a free fit parameter after subtracting the dark current of the camera from the measured spectra. The observation angle, θ, can be fitted freely as well or determined in dependence of B, as the magnetic field topology is sufficiently well known in W7-X [19]. By comparing the fitted B value with the nominal B values along each LOS, the radiation location along the LOS can be identified and the corresponding θ value at the same location is used. The nominal B and θ values are shown along the spectrometer LOS in section 5, figure 16. Although the view is restricted to a limited region of the W7-X divertor, B and θ vary considerably between and also along the LOS. Since the confining magnetic field of the W7-X stellarator is generated with external coils only, the topology of the W7-X magnetic field can be measured in vacuum to a very high degree of accuracy by magnetic flux surface measurements [19] for the various W7-X configurations. The vacuum flux measurements confirmed the theoretical field topology by the installed coil system and can be accessed via the W7-X field line tracer code [20]. During plasma operation, toroidal plasma currents are usually of the order of ± 10 kA [21] or less. These currents, located in the vicinity of the magnetic axis, induce changes to the magnetic field at the boundary by about $\Delta B \leqslant 1$ mT and $\Delta\theta \leqslant 0.01°$ along the spectrometer LOS. Thus, they fall well within the fitting accuracy of the routine and should not affect the fit results. Finite-β effects can be neglected for the plasmas that have been created so far in W7-X. They could, however, be present and considered in future W7-X plasma campaigns.

3.2. Error analysis and accuracy of the fit routine

The fitting of multiple parameters to measured data can become problematic if either

(a) several fit solutions exist or
(b) the signal-to-noise (S/N) ratio becomes too low.

Concerning the first point, fortunately, each of the four physics-related fit parameters, T_i, B, v_i and θ, have very different effects on the spectral line shape. This is illustrated in figure 8 in the example case of a He I transition, where B, θ and T_i were varied in the simulation. E.g. by increasing the magnetic field strength, the wavelength distance of the Zeeman-split components is increased, whereas by varying θ, the relative component intensities are changed with respect to each other. This is why, for successfully applying a fit approach with multiple parameters, it is necessary to spectrally resolve the Zeeman features of a measured line, preferably over the entire multiplet shape. The approach will not work if the Zeeman features are obscured by e.g. too high instrumental or thermal broadening. One such case is shown in figure 9, for the measured He II line around 468.5 nm: By varying the initial start parameters of the fit routine, different solutions are determined with indistinguishable line shape but significantly varying fit values. This is in contrast to many other, low-Z

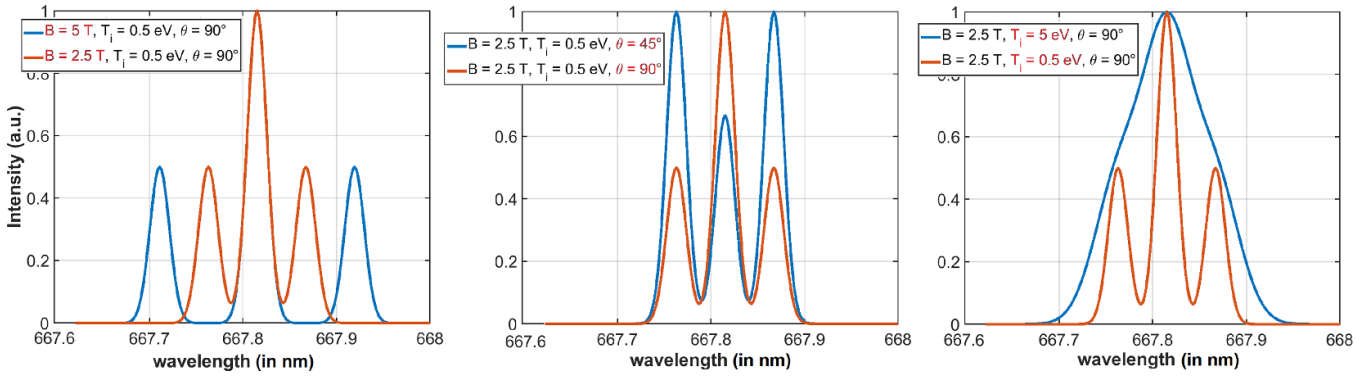

Figure 8. Simulated spectral line shapes for the He I line at 667.8 nm ($1s3d\ ^1D_2 \rightarrow 1s2p\ ^1P^\circ_1$) under consideration of Zeeman splitting, Doppler broadening and instrumental broadening of the spectrometer. The magnetic field strength B (left image), the observation angle θ (middle) and the particle temperature T_i (right) were varied to demonstrate their effects on the line-shape.

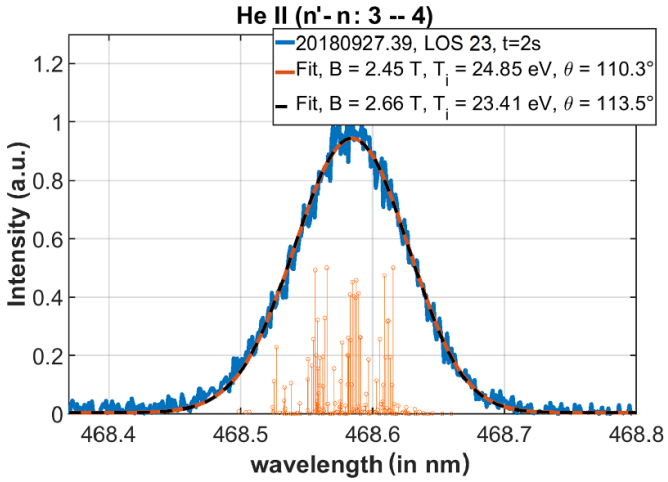

Figure 9. Passive He II spectrum measured with the high-resolution Echelle spectrometer (in blue) during a mixed hydrogen-helium plasma in W7-X along sightline number 23 (cf figure 6). Possible fit solutions for the line shape are shown in orange and black (dashed). They were determined by assuming different initial fit start parameters. Zeeman-split components are added as orange vertical lines, corresponding to the orange fit.

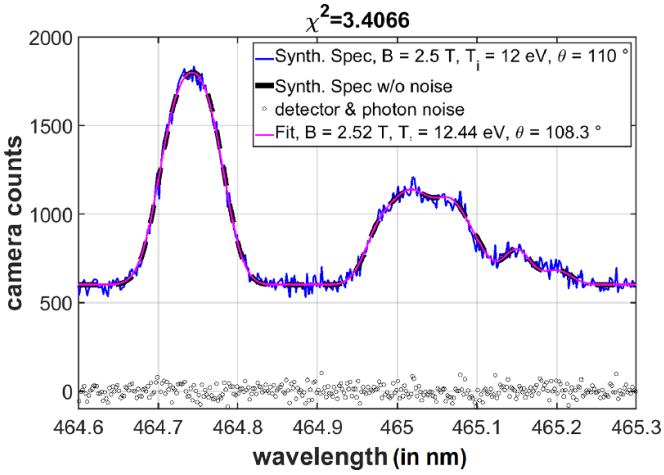

Figure 10. Simulated C III spectrum ($2s3p\ ^3P^\circ \rightarrow 2s3s\ ^3S$) (black dashed line) with medium artificial noise (blue), spectral variance (black markers), noise signal (white dots) and an exemplary fit (magenta).

impurity species with distinguishable Zeeman features that were investigated within the course of this work. He II has a relatively high excitation energy and therefore radiates at higher electron temperatures, which means it usually exists in SOL regions with higher T_i. At the given plasma conditions in the W7-X SOL, none of the numerous Zeeman-split components can be distinguished in the He II line shape, which resembles a single Gaussian. One cannot differentiate clearly between broadening by the Zeeman effect and thermal broadening. Therefore, in the case of He II, additional assumptions have to be made about the radiation location of the species, which determines the local B and θ values along the spectrometer LOS, and thus only T_i and v_i can be fitted freely.

The accuracy and validity of the fit results strongly depend on the S/N ratio of each analyzed spectrum. To characterize the accuracy of the fit routine, synthetic spectra are simulated where the 'true' spectral line parameters are known. Then, artifical white noise is added to the synthetic spectrum, as shown in an example case for the C III multiplet at 465 nm in figure 10. The temperature range usually observed for this line is around $T_i = 10$–15 eV, which is still low enough to observe Zeeman features (in contrast to He II). For the example, a magnetic field strength of $B = 2.5$ T, an ion temperature of $T_i = 12$ eV and an observation angle of $\theta = 110°$ were assumed. These are typical parameters for the C III transition along the spectrometer LOS. For the noise, Gaussian detector noise and photon noise are considered. By applying the fit routine for 1000 iterations on the same synthetic spectrum with varying random noise, the accuracy of the fit routine is characterized. Initial start parameters are $B = 2$ T, $T_i = 1$ eV and $\theta = 100°$. The resulting fit parameters for B, T_i, θ and the value

$$\chi^2 = \sum_{i=1}^{N} \frac{(y_i - Y_i)^2}{\sigma^2}, \tag{4}$$

where σ is the spectral variance, can be found in figure 11. Figures 10 and 11 demonstrate the example of a medium S/N

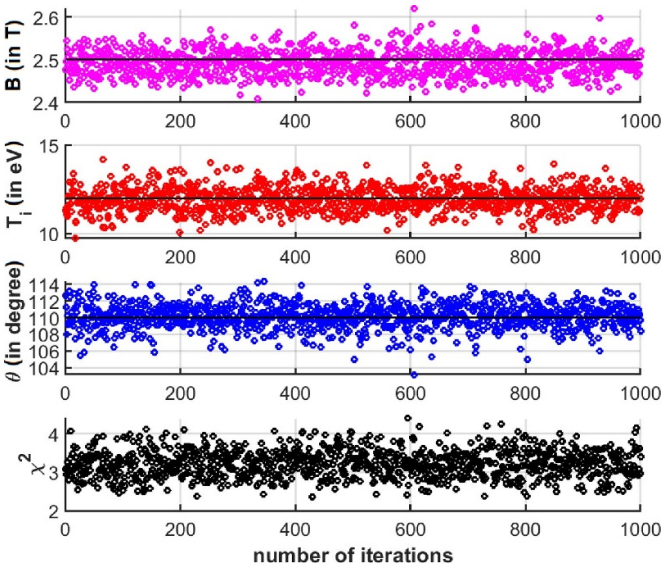

Figure 11. Fit results for a number of iterations with random, medium-level S/N for synthetic C III spectra, one example of which is presented in figure 10. The black lines in the first three plots indicate the chosen parameters for the synthetic spectrum.

Table 1. Overview of parameter uncertainty for the spectral fit routine for different S/N levels and spectral lines. The medium S/N parameter uncertainties are illustrated in figures 11 and 12 (right image).

	S/N (peak)	ΔB	ΔT_i	$\Delta\theta$	χ^2
C III	≈30 (high)	±0.04 T	±0.5 eV	±1.5°	≈1
C III	≈13 (medium)	±0.06 T	±2 eV	±4°	≈3.3
C III	≈7 (low)	±0.1 T	±3 eV	±7°	≈6.5
He I	≈11 (medium)	±0.02 T	±0.05 eV	±2°	≈0.7

ratio case, where the peak S/N ≈ 13. The fit results vary by roughly ±0.06 T for B, ±2 eV for T_i and ±4° for θ. This changes for a worse or better S/N ratio, as demonstrated in table 1. For higher S/N ratios, the uncertainties of all three physical parameters decrease. Therefore, for accurate line broadening analysis, it is necessary to increase the S/N ratio as much as possible for all sightline channels. However, the uncertainty of the fit results depends once more on the analyzed spectral line transition. Figure 12 shows a synthetic He I transition spectrum at 668 nm and the uncertainty of the fit parameters after 1000 iterations. For the same (medium) noise level, the uncertainty of the He I fit parameters is significantly smaller than for the C III multiplet (cf right image of figure 12). This is due to the different shape of the Zeeman features and the lower temperature of the species and this is also why the fit routine uncertainty needs to be investigated for each observed transition line individually.

In the next section, several different atomic impurity lines will be analyzed with the fit routine to investigate the impurity temperatures. In section 5, the possibility of emission localization via Zeeman spectroscopy is investigated for the case of the W7-X stellarator SOL. The uncertainty of the B and θ fits will be considered for this.

4. Impurity temperatures in the SOL of W7-X

In this section, highly-resolved spectra of various impurity emission lines are analyzed to derive impurity temperatures for various species via Doppler broadening. The measured spectra and their fits are presented in figures 13–15. Investigated impurity species include intrinsically present species (carbon, helium) and seeded impurities (argon and nitrogen). The focus is set to intense, low-Z transitions, which usually radiate very close to the divertor targets in attached plasma conditions. By considering both Doppler broadening and Zeeman splitting, values for the impurity temperatures, T_i, magnetic field strength, B, and observation angle, θ, are derived, which are stated in the upper right corner of each image in the figures and in table 2. The analyzed spectra were all measured during attached conditions, but in different plasma programs with varying plasma parameters and, in part, also magnetic field configurations. Nonetheless, all the shown spectra demonstrate that, by consideration of the magnetic field effects and thermal broadening, the measured spectral line shape can be reproduced reliably and used to infer ion temperatures. The fitted values of T_i are regarded as an upper limit, since the spectra are line-integrated.

In figure 13, two highly resolved wavelength spectra of the C III transition at 465 nm in the standard magnetic configuration are shown. This C III multiplet is one of the most intense impurity emission lines in the SOL of W7-X. Usually, in attached and detached conditions, the C^{2+} temperature in front of the divertor is fitted between $T_i \approx 10$–15 eV [11], as can be seen in the left image of figure 13. Since the S/N ratio is in the medium range, the uncertainty of the C^{2+} temperature is $\Delta T_i = \pm 2$ eV (cf table 1). The right image of figure 13 shows the C III spectrum from the same LOS during the same discharge later, when methane is puffed by the divertor gas inlet valves. Due to the methane puff, the carbon emission is significantly higher, which is why the S/N ratio improves substantially. The selected sightline lies close to gas inlet valve number 5 (cf figure 6), where the C^{2+} temperature locally decreases to $T_i \approx 6$ eV. The strong decrease of C^{2+} temperature is only observed along the LOS near the gas valves, further away it remains around 10–15 eV. The fitted values for B and θ are similar for both fits and correspond to the values of the magnetic field topology closest to the target plates along the LOS. The localization of the C III emission close to the targets during attached conditions is also observed in tomographic constructions performed by other spectrometers [22].

A spectrum from a lower ionization stage of carbon, C II, in the high-mirror magnetic configuration can be seen in the left image of figure 14. As example line, the C II transition around 514 nm was chosen for LOS 24, which ends on the vertical divertor target. The C II multiplet contains several components ranging from 513 nm to about 516 nm, which is a wider range than the high-resolution spectrometer is able to cover in one setting. Therefore, only a part of the multiplet was fitted. Furthermore, a small additional line around 514.8 nm is observed in the C II spectrum, which was disregarded in the fit. The derived particle temperatures are in the range of

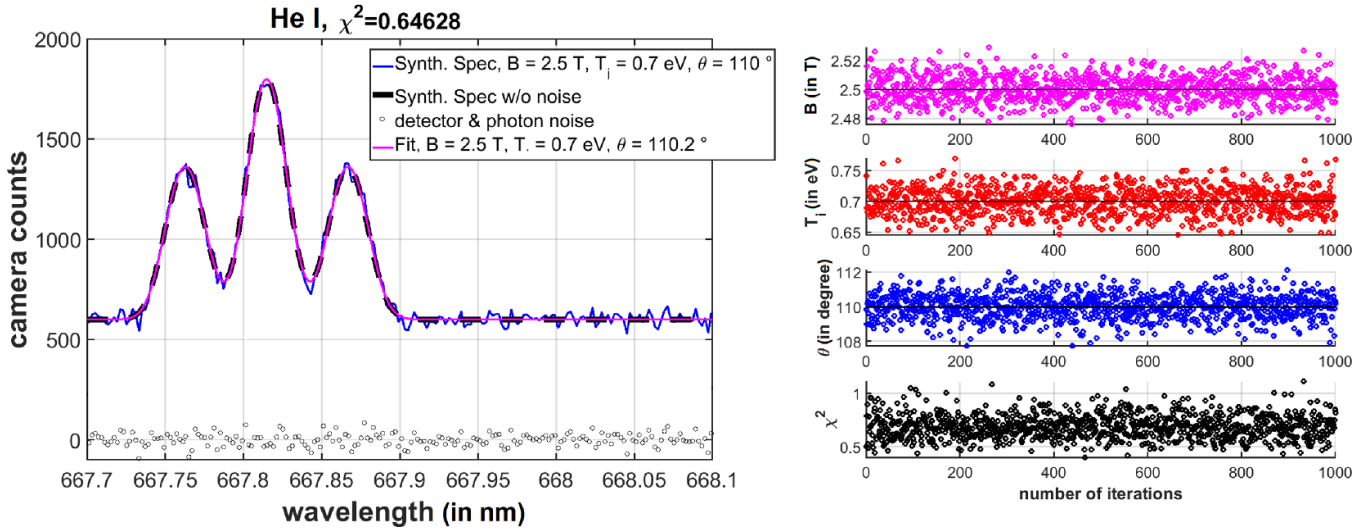

Figure 12. Left: simulated He I spectrum ($1s3d\ ^1D_2 \rightarrow 1s2p\ ^1P^\circ_1$) (black, dashed) with medium artificial noise (blue), spectral variance (black crosses), noise signal (black dots) and an examplary fit (magenta). Right: fit results for 1000 iterations with random, medium-level S/N for synthetic He I spectra, one example of which is presented in the left image. The black lines in the first three plots indicate the chosen parameters for the synthetic spectrum.

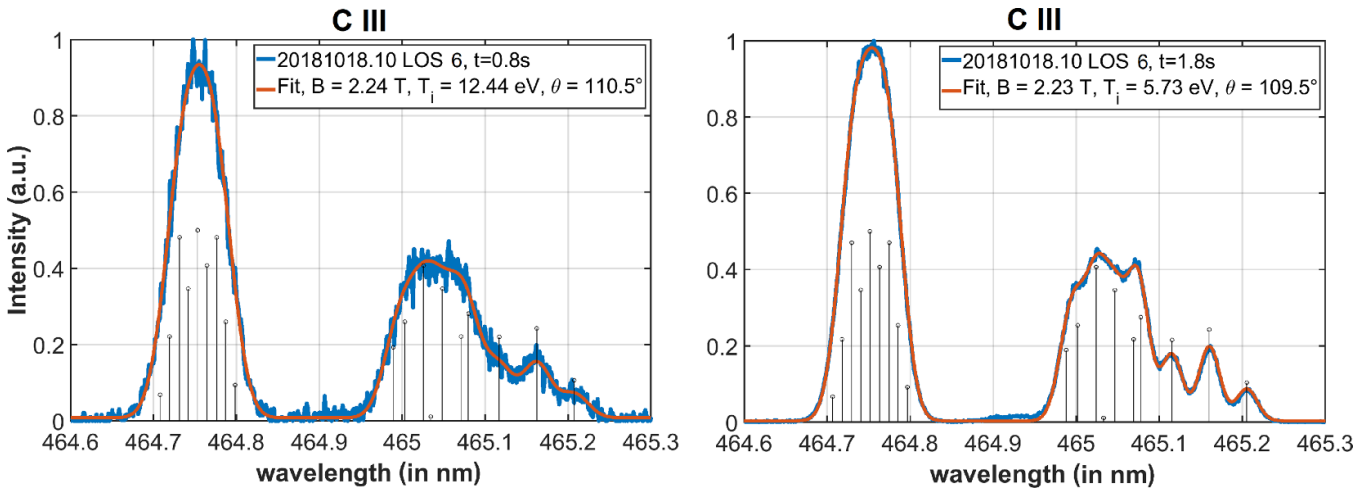

Figure 13. Measured (in blue) and fitted (in orange) C III spectra ($2s3p\ ^3P^\circ \rightarrow 2s3s\ ^3S$) before (left, at $t = 0.8$ s) and during a methane puff (right, at $t = 1.8$ s) from the gas inlet system of the divertor module monitored by the spectrometer. The exposure time of the spectrometer camera was set to 200 ms for both spectra. The fitted Zeeman-split components are added as black vertical lines.

$T_i = 5$ eV. These are lower fitted particle temperatures than for C III, which is to be expected [4].

Another interesting example is the He I line at 667.8 nm, which was measured in a W7-X series of plasma experiments with mixed helium-hydrogen content of roughly 50% each, in the standard magnetic configuration. As can be seen from the passively measured divertor spectrum in figure 14 (right image), a single line function is not sufficient to accurately fit the measured shape. The dominant part of the He I line is fitted with a low neutral temperature of $T_i < 1$ eV. The fit values for B and θ correspond to the magnetic field topology along the LOS at the targets. However, there is a second temperature component with higher temperature, that, presumably, originates from charge exchange recombination (CXR) collisions. The hot He* is characterized by a significant Doppler shift of 37 pm relative to the cold component, which corresponds to a velocity difference of 16.6 km s^{-1} and would support the origin of CXR. The fitted temperature of the hot He* component has a high uncertainty, since the Zeeman features of the line are not recognizeable. For the fit, the same Zeeman parameters (B, θ) have been assumed as for the cold neutral helium component. However, this assumption might not hold true if the charge exchange helium atoms radiate further upstream (where B and θ are different). This needs be investigated more deeply with tomographic reconstructions in the future.

Two examples for seeded induced impurity species are shown in figure 15 for the case of argon and nitrogen in the high-mirror magnetic configuration. The left spectrum was recorded when argon was puffed by the divertor gas inlet system of the divertor monitored by the spectrometer

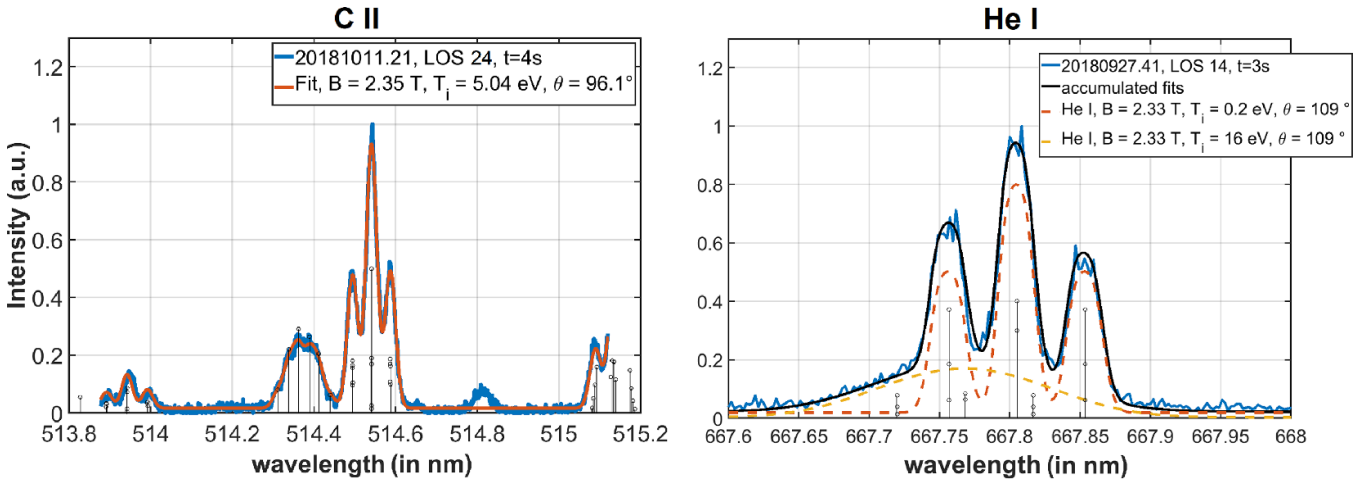

Figure 14. Measured and fitted C II ($2p3p\ ^4\mathrm{P} \rightarrow 2p3s\ ^4\mathrm{P}^\circ$) (left) and He I spectra ($1s3d\ ^1\mathrm{D}_2 \rightarrow 1s2p\ ^1\mathrm{P}_1^\circ$) (right). The He I transition was measured in a mixed helium-hydrogen plasma program and could not be adequately fitted with a single spectral function. A second simple gaussian-shaped component was assumed with 1/5 of peak radiation with respect to the main one. The fitted Zeeman-split components are added as black vertical lines.

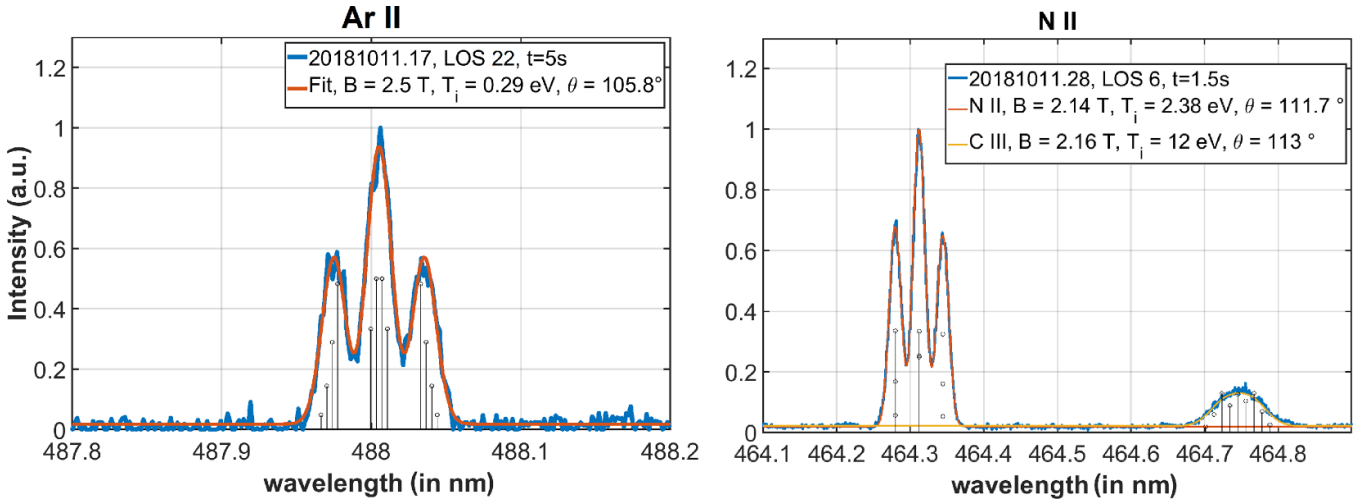

Figure 15. Measured and fitted spectrum of Ar II ($3p^44p\ ^2\mathrm{D}^\circ \rightarrow 3p^44s\ ^2\mathrm{P}$) (left) and N II ($2p3p\ ^3\mathrm{P} \rightarrow 2p3s\ ^3\mathrm{P}^\circ$) (right). Both impurities were seeded by the divertor gas inlet system shown in figure 6. The fitted Zeeman-split components are added as black vertical lines.

(see figure 6). The exposure time of the spectrometer camera was 1 s. Over the plasma discharge, a clear rise in Ar II intensity was observed by the spectrometer LOS. However, the strongest localization of the Ar II line was measured by the LOS ending on the vertical divertor target plates, indicating that the Ar II distributed along the open magnetic field lines and was not localized around the gas valves, possibly related to argon being a highly recycling impurity. The fitted Ar II temperature is particularly low at $T_i \approx 0.3$ eV. One could indeed expect argon ions to be the coldest, since the ratio of nuclear to proton mass is the greatest of those elements analyzed here. Hence, nuclear collisional heating is the least effective.

This behavior is different from that of nitrogen, which was also puffed through the same gas valve but was more localized around its seeding location. Similar to carbon, it is not a strong recycling impurity. In figure 15 (right image), a N II spectrum is shown from LOS 6, which lies in the proximity of the divertor gas inlet valve number 5. The N II transition is a multiplet with several components ranging between 460 and 465 nm. With the spectral setting centered at 464.3 nm, only the N II component at that location could be observed from the entire transition with the high-resolution spectrometer. Next to it, around 464.7 nm, is the highest peak of the C III multiplet shown in figure 13. For LOS 6, N II intensity was highest among the spectrometer LOS and even more intense than the intrinsic C III emission line. The N II fit suggests an impurity temperature higher than for Ar II, around $T_{i,N^{1+}} \approx 2$ eV. The fit values for B and θ agree with the magnetic field topology at the targets.

An overview of the temperatures of all investigated, weakly ionized impurity species can be found in table 2. Even though they are all located close to the divertor targets in attached conditions, according to the fitted B and θ values, their fitted temperatures vary from each other. This is in agreement with observations made in tokamaks, such as in TEXTOR [4]. A competition between ion-ion collisional heating and

Table 2. Overview of the temperature fit results for the five investigated transition lines observed with the Echelle spectrometer in the SOL of W7-X. λ_0 is the unshifted center-of-mass wavelength in air for the spectral transition.

Ion	Transition	λ_0 (in nm)	Temperature
He I	$1s3d\ ^1\mathrm{D}_2 \rightarrow 1s2p\ ^1\mathrm{P}_1^\circ$	667.82	0.2 eV
Ar II	$3p^4 4p\ ^2\mathrm{D}^\circ \rightarrow 3p^4 4s\ ^2\mathrm{P}$	487.73	0.3 eV
N II	$2p3p\ ^3\mathrm{P} \rightarrow 2p3s\ ^3\mathrm{P}^\circ$	462.32	2.3 eV
C II	$2p3p\ ^4\mathrm{P} \rightarrow 2p3s\ ^4\mathrm{P}^\circ$	514.19	5 eV
C III	$2s3p\ ^3\mathrm{P}^\circ \rightarrow 2s3s\ ^3\mathrm{S}$	464.88	10–15 eV

electron-ion collisional ionization determines the temperature of a particular ion species [23]. Electron-ion collisional ionization leads to the fast annihilation of the lower ionization stages of impurities. As a consequence, especially for sputtered impurities like carbon, low charge states should have temperatures below those of the background protons, as explained more detailed in [4, 15] (see figure 13 in the latter reference).

5. Localization of line radiation

This section addresses the question under which circumstances Zeeman spectroscopy can be used for emission localization in the W7-X stellarator. Since Zeeman splitting of atomic emission lines is dependent on the magnetic field strength $|B|$ as well as the observation angle θ, in theory, passive Zeeman spectroscopy could be used to localize the emission in a high-temperature magnetic confinement experiment. However, to our knowledge, this is rarely done or reported in practice, which might be due to one or several of the following reasons:

(a) Passive Zeeman spectroscopy can only work (in the SOL) when emitting particle species are cold enough for the Zeeman splitting to become significant (or even dominant) for the spectral line shape.
(b) The magnetic field strength, $|B|$, and the magnetic field topology, $\vec{B}$, need to be known to a high degree of accuracy along the spectrometer LOS.
(c) The line emission needs to be localized in a small region along the LOS.

The first point further implies a high-wavelength resolution spectrometer in order to resolve the Zeeman features, as explained in the introduction. Concerning the second point, precise knowledge of the edge magnetic field is generally difficult to achieve in the edge of tokamaks, where the magnetic field topology is derived with equilibrium codes. In contrast, stellarators such as W7-X provide a unique opportunity: $|B|$ and $\vec{B}$ are obtained by magnetic field-line mapping, a sensitive technique to measure the detailed topology of magnetic surfaces when the stellarator field is generated in vacuum without plasma. This method verified the magnetic topology down to errors on the order of 10^{-4} in the W7-X standard and high-mirror configurations (i.e. b_{11} and b_{22} components) [24, 25]. Even in case of non-negligible bootstrap currents (of the order of a few kA) developing during the plasma discharge, the magnetic topology can be determined with a precision of $\delta B_M = 1$ cm based on the magnetic field line mapping measurements. In addition, finite β-values will also alter the magnetic structure, especially the size and position of the magnetic of the magnetic edge islands. Because of the low values reached so far in the last operation phase, OP1.2, the topic is beyond the scope of this article.

Concerning the third point, atomic line emission can be distributed over a large part of the SOL in the edge island topology of W7-X. EMC3-Eirene simulations during e.g. detachment [26] determine a relatively homogeneous distribution of line radiation along the last closed flux surface, which is also confirmed by coherence imaging measurements for C III (see figure 5 in [27]). This is in contrast to tokamaks SOLs, where emission is mainly localized in the divertor area around the X-Point [28, 29] in a divertor configuration. In W7-X, it is possible that spectrometer LOS collect emission from different regions of the SOL, depending on the view, magnetic field configuration and plasma parameters. Therefore, in this section, the fit routine accuracy is investigated with regard to emission localization in case of one or two emission regions along the LOS.

In figure 16, the values of B and θ are shown for the standard configuration along the 27 LOS of the high resolution spectrometer. The field data was obtained via the W7-X field line tracer code [20]. Both B and θ vary considerably along the LOS, e.g. in the poloidal direction in the divertor area, B increases from 2.3 to 2.6 T along the target surfaces and pumping gap. Furthermore, both parameters have a local maximum in the core of the plasma, thus not being unique along the LOS. For this reason, if θ is determined in dependence of B, the fit range must be limited to either the divertor or the SOL region in front of the observation window.

By analyzing the magnetic field data from the field line tracer, it was found that e.g. along LOS number 1, a change of 0.1 T roughly corresponds to a variation of 14.7 cm along the LOS in the divertor area. This means that an uncertainty of e.g. 0.04 T, as in the case of high S/N ratio for the C III line (cf table 1 in the previous section), translates into an uncertainty of 5.9 cm in the emission localization along the LOS. This accuracy is sufficient for e.g. observing whether the radiation is close to the targets (as it is usual in attached conditions) or close to the last-closed flux surface (LCFS) during detached conditions, as was investigated in [11]. This is possible because the distance between the targets and the LCFS varies between 17 cm (LOS 1) and 9 cm (LOS 10) along the LOS in the divertor area. In case of one predominant emission region, the C III emission localisated with the fit routine has an uncertainty of few centimeters along the LOS, depending on the S/N ratio. Considering the uncertainties of the fit parameters for the C III line, even with good S/N ratios, passive Zeeman spectroscopy is not accurate enough to e.g. determine whether the C III emission occurs in- or outside of the LCFS during detachment for typical C^{2+} temperatures between 10 to 15 eV. However, this might differ for other transitions, as, for example, the He I line, where the uncertainty for B is

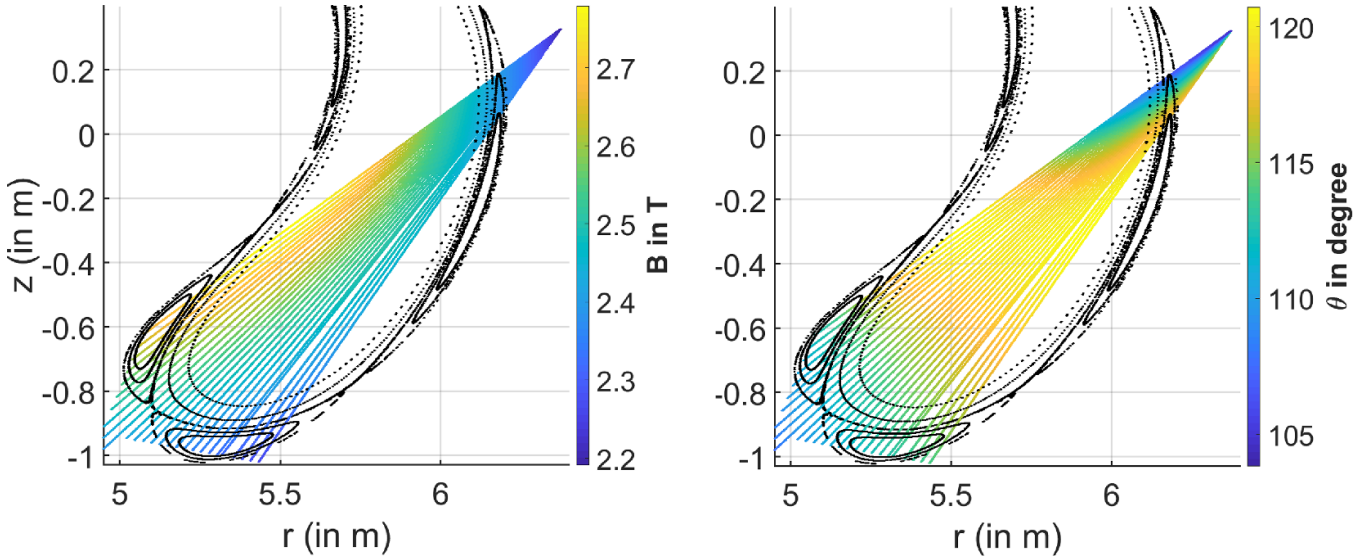

Figure 16. Variation of the magnetic field strength (left image) and the observation angle (right) along the 27 spectrometer LOS in use during the analysis of this work. The values are representative for the standard magnetic configuration with $B = 2.6$ T on the main axis. A Poincaré plot of the magnetic island topology in the plane of the LOS is indicated in black, at a toroidal angle of $\phi \approx 12°$.

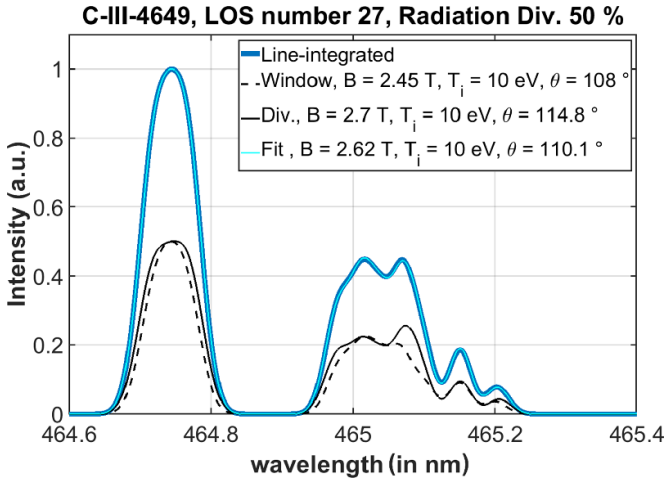

Figure 17. Two simulated C III spectra (black, continuous and dashed) in the divertor area and in front of the window region along LOS 27 (cf figure 6). For the line-integrated spectra (blue), both spectra were weighted with 50% each. The result fit of the line-integrated spectra is shown in cyan.

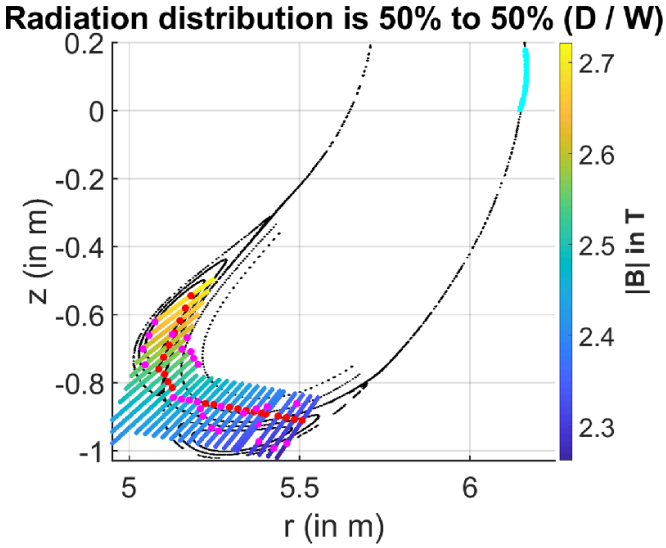

Figure 18. Localized emission along the 27 vertical LOS (magenta) in the divertor area of W7-X, for a synthetic, line integrated spectrum composed of two emission areas (cf figure 17). The red and and cyan dots indicate the selected positions of the synthetic spectra in the divertor and in front of the window, respectively. The allowed fit range for the spectrum is indicated by the visualization of the magnetic field strength, B, along the spectrometer LOS.

$\Delta B = 0.02$ T. He I can therefore be localized with an uncertainty of ± 3 cm along the vertical LOS.

First tomographic analysis results via medium-resolution spectroscopy [22] report the presence of at least two emission zones in detached plasmas in the SOL of W7-X for both C II and C III. Therefore, synthetic spectra were also used to study the accuracy of the fit routine in case of two (line-integrated) emission zones along the LOS. Figure 17 shows a line-integrated spectrum generated out of two synthetic spectra, one radiating in front of the observation window (where $B = 2.45$ T and $\theta = 108°$) and one close to the divertor plates ($B = 2.7$ T and $\theta = 114.8°$) along LOS 27. The locations of the synthetic spectra in the W7-X SOL are also visualized in figure 18. For both spectra, the same ion temperature of $T_i = 10$ eV was assumed and no noise effects were considered, for simplicity. If only one spectrum is used to fit the line-integrated combined spectrum, a good fit can be determined with values of $B = 2.62$ T and $\theta = 110.1°$, that lie in between the values of the two synthetic spectral components. Thus, the fit routine is able to accurately reproduce two line-integrated spectra with just a single spectrum, albeit with fit parameters that neither agree with the window nor the divertor spectrum. This was also confirmed by fits for the other LOS.

When fitting the line-integrated spectrum with two spectra, the two synthetic spectra cannot always be accurately reproduced. At first, a fit routine was applied where B, T_i as well as the amplitudes of both spectra could be freely fit by the routine. Then, the fitted parameters were more limited, so that only the amplitude of the window emission was fit, whereas B and T_i were fixed. In both scenarios, there are deviations of the fit results that lead to e.g. the wrong emission localization among most of the spectrometer LOS, as shown in figure 18. In case of two emission zones along the vertical LOS, three fit parameters (B, T_i in the divertor, as well as the amplitude ratio of the divertor and window spectrum) or more allow no unique fit solution. Additional tomographic information by e.g. other diagnostics is necessary to provide constraints to the fit parameters. In future, this could be achieved by divertor tomography [22] to derive an amplitude ratio for the window and divertor emission.

Altogether, it is concluded that successful radiation localization in W7-X via Zeeman spectroscopy suffers from the homogeneous radiation distribution in the SOL island topology, even though we benefit from a very accurate magnetic field database. If two emission zones exist with similar temperatures, Zeeman spectroscopy cannot really differentiate whether one or two spectra are present. Only in the case of two emission zones with very different temperature components, as observed for the measured He I transition line at 668 nm (cf figure 14), two line functions can be accurately fit to the data.

6. Summary and conclusions

A first line-broadening analysis has been carried out for spectral impurity emission lines in the divertor SOL of W7-X. Atomic line emission for cold edge impurities is significantly characterized by both Doppler broadening and Zeeman splitting, due to the low temperatures in the SOL ($T_i < 100$ eV) and the confining magnetic field in W7-X ($B = 2.5$ T). A high-wavelength resolution spectrometer with narrow instrumental broadening is necessary to spectrally resolve the Zeeman features for the various SOL spectral lines. For the line broadening analysis of the measured spectra, a routine fitting multiple parameters was implemented. It is able to derive impurity temperatures, $T_{i,Z}$, from Doppler broadening and the magnetic field strength, B, and observation angle, θ, at the emission location along the spectrometer LOS due to Zeeman splitting. The fit routine is able to reproduce the line shape of several impurity lines accurately. Uncertainties of the derived values vary for each atomic line individually and depend on the S/N ratio of the measured spectra.

For intrinsic carbon in the divertor region, the temperature for C^{1+} is $T_{i,C} \approx 5$ eV and increases to $T_{i,C} \approx 10$ to 12 eV for C^{2+} in typical attached conditions in W7-X. For seeded impurities through the divertor gas inlet system, Ar^{1+} and N^{1+}, lower temperatures have been measured than for C^{1+}, at $T_{i,Ar} < 1$ eV and $T_{i,N} = 2$ eV, respectively. Furthermore, a neutral helium transition line was analyzed in a mixed hydrogen-helium plasma program. Two temperature components could be observed in the spectrum, one cold component ($T_{n,He} < 1$) and a hotter one, which is assumed to originate from CXR collisions.

Since the spectral line broadening analysis also yields values for B and θ, radiation localization is possible under certain conditions, because the magnetic field topology is very accurately known in W7-X. Careful investigation is required as to whether emission occurs locally along the spectroscopic LOS or at several positions. The W7-X island SOL is characterized by several X- and O-points in each poloidal cross-section, which leads to a more homogenous radiation distribution than in tokamaks. For the observation directions used in this work, emission can occur twice along the LOS. If two spectra with similar temperatures become line-integrated along the LOS, it is not possible to use the spectra for emission localization via Zeeman spectroscopy without additional tomographic information. A more detailed study of the radiation distribution of various impurity species is therefore necessary to evaluate the applicability of the fit routine for emission localization via Zeeman spectroscopy for future investigations. This investigation could either be carried out by Gaussian Process Tomography [22] or the new divertor bolometry diagnostic planned for the next operation phase, OP2.1.

Data availability statement

The data that support the findings of this study are available upon reasonable request from the authors.

Acknowledgments

The corresponding author is very grateful for the help of the retired Mr Jean-Louis Stehlé from the former Sopra company. Mr. Stehlé visited our laboratory and helped us to calibrate and set-up the Ebert Fastie spectrograph for Wendelstein 7-X, after 10 years of non-use. Additionally, the authors would like to express their deep gratitude to John D Hey, who provided an algorithm for determining the Zeeman splitting and assisted this work with a lot of helpful comments and explanations about Zeeman spectroscopy.

This work has been carried out within the framework of the EUROfusion Consortium, funded by the European Union via the Euratom Research and Training Programme (Grant Agreement No. 101052200 — EUROfusion). Views and opinions expressed are however those of the author(s) only and do not necessarily reflect those of the European Union or the European Commission. Neither the European Union nor the European Commission can be held responsible for them.

ORCID iDs

D Gradic https://orcid.org/0000-0002-6109-9345
M Otte https://orcid.org/0000-0003-3134-7579
V Perseo https://orcid.org/0000-0001-8473-9002
T Sunn Pedersen https://orcid.org/0000-0002-9720-1276

References

[1] Stangeby P C 2000 *The Plasma Bounday of Magnetic Fusion Devices (Plasma Physics Series)* (Bristol: Institute of Physics Publishing)

[2] Kocan M *et al* 2011 Measurements of ion energies in the tokamak plasma boundary *J. Nucl. Mater.* **415** S1133–8

[3] Li Y *et al* 2019 Measurement of the edge ion temperature in W7-X with island divertor by a retarding field analyzer probe *Nucl. Fusion* **59** 126002

[4] Hey J D, Lie Y T, Rusbüldt D and Hintz E 1994 Doppler broadening and magnetic field effects on some ion impurity spectra emitted in the boundary layer of a Tokamak plasma *Contrib. Plasma Phys.* **34** 725–47

[5] Hey J D, Chu C C and Brezinsek S *et al* 2001 Oxygen ion impurity in the TEXTOR-94 boundary plasma observed by Zeeman Spectroscopy *28th EPS Conf. on Control. Fusion and Plasma Phys. Funchal* vol 25A (ECA) pp 353–6

[6] Barbui T *et al* 2020 Measurements of plasma parameters in the divertor island of Wendelstein 7-X through line-ratio spectroscopy on helium *Nucl. Fusion* **60** 106014

[7] Henderson S S, Bernert M, Brezinsek S , Carr M, Cavedon M, Dux R, Lipschultz B, O'Mullane M G, Reimold F, Reinke M L 2018 Determination of volumetric plasma parameters from spectroscopic N II and N III line ratio measurements in the ASDEX Upgrade divertor *Nucl. Fusion* **58** 016047

[8] Pavone A *et al* 2019 Measurements of visible bremsstrahlung and automatic Bayesian inference of the effective plasma charge Z_{eff} at W7-X *J. Instrum.* **14** C10003

[9] Ford O P *et al* 2020 Charge exchange recombination spectroscopy at Wendelstein 7-X *Rev. Sci. Instrum.* **91** 023507

[10] Banerjee S, Kumar V, Chowdhuri M B , Ghosh J, Manchanda R, Patel K M and Vasu P 2008 Space- and time-resolved visible-emission spectroscopy of Aditya-tokamak discharges using multi-track spectrometer *Meas. Sci. Technol.* **19** 045603

[11] Gradic D *et al* 2021 2D coherence imaging measurements of C^{2+} ion temperatures in the divertor of Wendelstein 7-X *Nucl. Fusion* **61** 106041

[12] Fastie W G 1991 Ebert spectrometer reflections *Phys. Today* **44** 37–43

[13] Gradic D, Perseo V, König R and Ennis D 2019 A new calibration implementation for Doppler coherence imaging spectroscopy *Fus. Eng. Des.* **146** 995–8

[14] Perseo V, Gradic D, König R, Ford O P, Killer C, Grulke O and Ennis D A 2020 Coherence imaging spectroscopy at Wendelstein 7-X for impurity flow measurements *Rev. Sci. Instrum.* **91** 013501

[15] Hey J D, Chu C and Mertens P 2002 Zeeman spectroscopy as a tool for studying atomic processes in edge plasmas *Contrib. Plasma Phys.* **42** 635–44

[16] Hey J D, Chu C C, Brezinsek S, Mertens P and Unterberg B 2002 Oxygen ion impurity in the TEXTOR tokamak boundary plasma observed and analysed by Zeeman spectroscopy *J. Phys. B: At. Mol. Opt. Phys.* **35** 1525–53

[17] Hey J D, Chu C C, Mertens P , Brezinsek S and Unterberg B 2004 Atomic collision processes with ions at the edge of magnetically confined fusion plasmas *J. Phys. B: At. Mol. Opt. Phys.* **37** 2543–67

[18] Summers H 2004 The ADAS user manual, version 2.6 (available at: www.adas.ac.uk)

[19] Sunn Pedersen T, Otte M and Lazerson S *et al* 2016 Confirmation of the topology of the Wendelstein 7-X magnetic field to better than 1:100,000 *Nat. Commun.* **7** 13493

[20] Bozhenkov S A, Geiger J, Grahl M , Kißlinger J, Werner A and Wolf R C 2013 Service oriented architecture for scientific analysis at W7-X. An example of a field line tracer *Fusion Eng. Des.* **88** 2997–3006

[21] Killer C *et al* 2019 Effect of toroidal plasma currents on the Wendelstein 7-X scrape-off layer *Plasma Phys. Control. Fusion* **61** 125014

[22] Krychowiak M *et al* 2021 Gaussian process tomography of carbon radiation in the transition to detached plasmas in the Wendelstein 7-X stellarator vol 45A *47th EPS Conf. on Plasma Physics (Conf. Proc.)* P1.1026

[23] McCracken G M *et al* 1990 A study of impurity transport in the plasma boundary of TEXTOR using gas puffing *J. Nucl. Mater.* **176-177** 191

[24] Bozhenkov S, Otte M, Biedermann C , Jakubowski M, Lazerson S A, Sunn Pedersen T and Wolf R C 2019 Measurements and correction of the 1/1 error field in Wendelstein 7-X *Nucl. Fusion* **59** 026004

[25] Lazerson S A *et al* 2018 Error fields in the Wendelstein 7-X stellarator *Plasma Phys. Control. Fusion* **60** 124002

[26] Feng Y *et al* 2021 Understanding detachment of the W7-X island divertor *Nucl. Fusion* **61** 086012

[27] Perseo V *et al* 2021 2D measurements of parallel counter-streaming flows in the W7-X scrape-off layer for attached and detached plasmas *Nucl. Fusion* **61** 116039

[28] Potzel S, Wischmeier M, Bernert M , Dux R, Müller H W and Scarabosio A 2014 A new experimental classification of divertor detachment in ASDEX Upgrade *Nucl. Fusion* **54** 013001

[29] Kallenbach A *et al* 2015 Partial detachment of high power discharges in ASDEX Upgrade *Nucl. Fusion* **55** 053026